High-temperature oxidation of CoGa: Influence of the crystallographic orientation on the oxidation rate

U. Koops
Institute of Physical Chemistry, Darmstadt University of Technology, Petersenstraße 20, D-64287 Darmstadt, Germany

D. Hesse
Max Planck Institute of Microstructure Physics, Weinberg 2, D-06120 Halle, Germany

M. Martin[a)]
Institute of Physical Chemistry I, Aachen University of Technology (RWTH), Templergraben 59, D-52056 Aachen, Germany

(Received 8 February 2002; accepted 10 June 2002)

The crystallographic orientation plays an important role in high-temperature oxidation of the intermetallic compound CoGa. When CoGa is exposed to air at elevated temperatures, the oxide β–Ga_2O_3 is formed, and different scale growth rates are observed, depending on the crystallographic orientation of the CoGa grains. This dependence is a consequence of the anisotropy of the gallium diffusion rate through the β–Ga_2O_3 scale and of a topotaxial orientation relationship occurring between β–Ga_2O_3 and CoGa. The combination of *ex situ* techniques, such as transmission electron microscopy and electron backscatter diffraction with optical microscopy, applied *in situ* resulted in a thorough understanding of these relations and of the oxidation process in general.

I. INTRODUCTION

The intermetallic compound CoGa shows an excellent high-temperature oxidation resistance. When exposed to air at elevated temperatures, Ga is selectively oxidized, and a compact and dense oxide scale of β–Ga_2O_3 forms. Through time-resolved, *in situ* x-ray powder diffraction it could be shown that after an induction period the scale growth follows a simple parabolic rate law.[1–3] This means that the rate determining step is diffusion through the oxide layer. During the oxidation process pores are formed in the intermetallic CoGa at the metal/oxide interface. This observation gives clear evidence that β–Ga_2O_3 grows by diffusion of Ga ions from the metal/oxide to the oxide/gas interface. Diffusion of oxygen ions in the opposite direction can be excluded, since in this case β–Ga_2O_3 would grow at the metal/oxide interface and no pores could grow (they would be filled by the growing oxide). β–Ga_2O_3 is known to be a semiconductor;[4,5] thus it can be concluded that β–Ga_2O_3 grows by ambipolar diffusion of Ga ions and electronic defects through the oxide scale,[1–3] resulting in the observed parabolic rate law as described by Wagner's oxidation rate theory.[6]

Since β–Ga_2O_3 has an anisotropic crystal structure as described below, an orientation dependence of the gallium diffusion rate through the oxide can be expected, which in turn should result in different rates of scale growth for different crystallographic orientations of the oxide. The orientation of the forming oxide can in turn be expected to depend on the orientation of the underlying metal substrate, at least if a topotaxial oxidation mechanism occurs. This expectation is supported by studies of the very early oxidation states of CoGa.[7–9] However, these experiments were performed under high vacuum conditions, and single-crystalline samples of CoGa were exposed to small amounts of oxygen corresponding to coverages in the monolayer regime. The resulting islands of β–Ga_2O_3 were analyzed by low energy electron diffraction (LEED) showing certain orientation relationships (see below). As a result, it appears that the rate of high-temperature oxidation of CoGa should depend on its crystallographic orientation, resulting in a different scale thickness on differently oriented grains of a polycrystalline CoGa intermetallic. A better knowledge of these relations is necessary if one aims at an optimization of the oxidation resistance of CoGa. With this goal in mind, experimental investigations on polycrystalline CoGa samples were performed, in which the rate of scale growth in dependence on the crystallographic orientation of the CoGa grains was studied.

II. EXPERIMENTAL

A. Applied methods

To study the influence of sample orientation on the growth rate of the oxide scale, the crystallographic orientation of the respective metal sample must be known. Depending on the method of determining the growth

a)Address all correspondence to this author.

kinetics, different possibilities exist, which required samples of different types. For example, if thermogravimetry or *in situ* x-ray diffraction is used to follow the oxidation rate, a number of single-crystal samples with differently oriented surfaces must be cut and polished. This is elaborate, and, moreover, the above methods do not allow determination of the oxide layer thickness with any sensible lateral resolution because the measured signal is integral over the whole sample. Less-elaborate experiments are possible if polycrystalline samples are used, provided that the crystallographic orientation of the individual grains can be determined and the growth rate of the scale can be measured with sufficient spatial resolution.

A method that reveals the scale thickness with high lateral resolution, and in addition allows determination of the orientation relationships, is transmission electron microscopy (TEM) in combination with selected-area electron diffraction (SAED). The TEM investigations were performed in a standard transmission electron microscope with 200-keV primary beam energy, equipped with a 45° double-tilt holder (CM20T, Philips, Eindhoven, The Netherlands). This method can, however, be applied only after oxidation, i.e., as an *ex situ* technique. To measure the oxidation rate during oxidation in dependence on the grain orientation of the polycrystalline intermetallic substrate, a method with a spatial resolution better than the grain size of the metal has to be used. In polycrystalline CoGa samples obtained by arc melting, the grain size varies from 10 to 1000 μm. Thus optical microscopy is a suitable method, provided that the required temperatures can be reached and maintained in the microscope during the measurement. We chose this option, measuring the thickness of the oxide scale on polycrystalline CoGa samples via the interference colors of the scale. The experiments were performed *in situ* in a specially designed hot stage adapted to an optical microscope (Leica DMRM, Germany). The orientation of the CoGa grains was determined prior to the oxidation experiments by electron backscatter diffraction (EBSD) via selected-area channeling (SAC) in a scanning electron microscope (SEM; Zeiss 962, Germany), equipped with a special beam control for SAC, and via orientation mapping (demonstration laboratory of Oxford Instruments, Wiesbaden, Germany).

B. Sample preparation

Polycrystalline samples of the intermetallic compound CoGa were obtained by arc melting the elements Co and Ga under argon in the desired stoichiometric ratio. The phase purity of the samples was checked by x-ray diffraction (XRD), and analysis of the stoichiometry was performed using SEM energy dispersive x-ray (EDX), electron probe microanalysis (EPMA), as well as a wet chemical analysis (atomic absorption spectroscopy, AAS). All samples used in this study have a slight Co-excess ($Co_{52.6\pm0.2}Ga_{48.3\pm0.3}$), but they will always be denoted "CoGa." Disks were cut from the ingots with a diamond wire saw (Well, Mannheim, Germany). Grinding and polishing were performed by standard metallographic methods, whereby SiC papers and a diamond polishing paste were used to reduce the surface roughness. The final polishing step was performed using an alumina-silica suspension of 60-nm grain size (Mastermet I, Wirtz-Buehler, Düsseldorf, Germany) on a velvet disc. For the TEM investigations, thin plan-view and cross-sectional specimens were prepared by mechanical polishing and subsequent argon ion milling (DuoMill, Gatan, München, Germany) following the well-known established techniques; see Ref. 10.

III. RESULTS

A. TEM investigations

1. Crystallographic orientations and topotaxial relationships

The lattice parameters and space groups of the involved materials, i.e., CoGa and β–Ga_2O_3, are shown in Table I.[11,12] A number of interplanar distances and angles common to both CoGa and β–Ga_2O_3 can be found (Sec. III), which make the presence of a topotaxial orientation relationship most probable. Accordingly, an investigation of the crystallographic orientation of the β–Ga_2O_3 scale relative to the underlying CoGa grain(s) was carried out by SAED in TEM.

Figure 1(a) shows a bright-field cross-sectional image of the gallium oxide scale developed on a CoGa grain during 24 h of oxidation at 800 °C in air. The entire CoGa region imaged in Fig. 1(a) belongs to one CoGa grain. While the oxide/metal interface is smooth and planar (except for the presence of pores, the role of which is considered below), the surface of the oxide scale is rather rough, most probably due to the surfacial facets of the columnar grains forming the scale. On average, the thickness of the oxide scale is 135 nm. The columnar structure of the oxide scale is particularly easy to see in the dark-field image [Fig. 1(b)]; the width of a column is on the order of 30 nm (for the different brightness of the columns, see below). A closer inspection of these and other TEM images reveals the presence of many planar defects, most probably stacking faults, in addition to the boundaries between the columnar grains. The fact that

TABLE I. Crystallographic parameters of the involved materials CoGa and β–Ga_2O_3.[11,12]

Material	Space group	Lattice parameters	
CoGa	*Pm3m* (No. 221)	$a = b = c = 0.2878$ nm	$\alpha = \beta = \gamma = 90°$
β–Ga_2O_3	*C2/m* (No. 12)	$a = 1.2214$ nm	$\alpha = \gamma = 90°$
		$b = 0.3037$ nm	$\beta = 103.87°$
		$c = 0.5798$ nm	

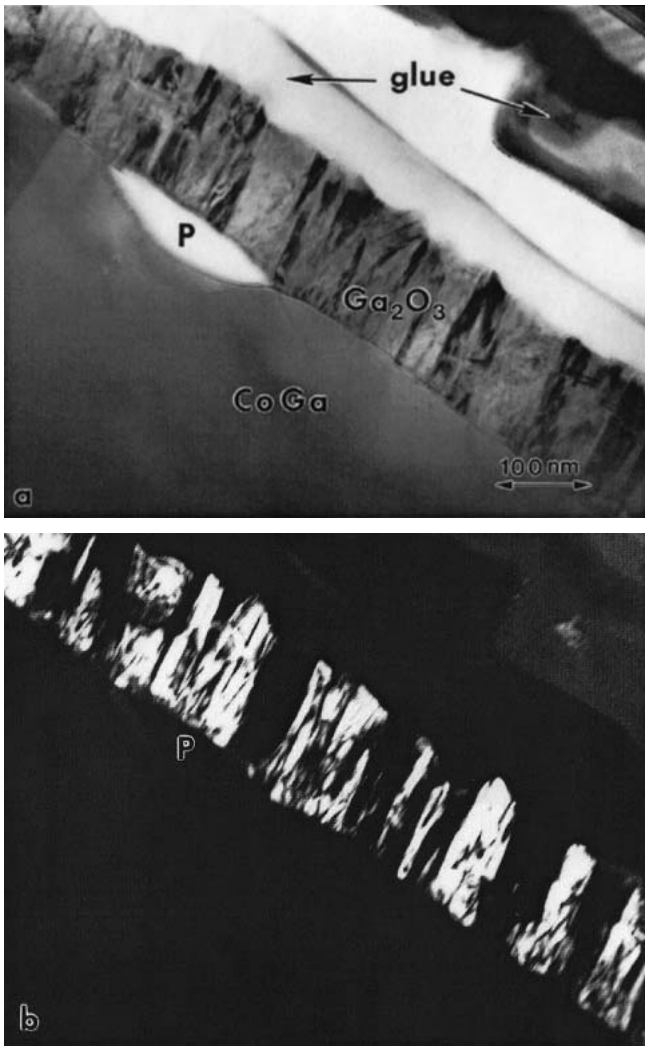

FIG. 1. (a) Cross-sectional bright-field TEM and (b) β–Ga_2O_3 dark-field image of the β–Ga_2O_3 scale developed on a grain of the intermetallic compound CoGa during 24 h of oxidation at 800 °C in air. P designates a pore formed at the oxide/metal interface.

the long axis of the columns makes a definite angle around 80° with the substrate plane already points to a definite orientation relationship of the oxide with respect to the metal grain. This relationship was analyzed by SAED using various definite tilts of the specimen in a 45° double tilt holder.

Figures 2(a) and 2(b) show two of the SAED patterns obtained, together with schematic patterns in Figs. 2(c) and 2(d), which display the locations of the CoGa and β–Ga_2O_3 reflections and their (*hkl*) indices. From an analysis of these and other diffraction patterns, taking the well-known magnetic rotation between images (Fig. 1) and diffraction patterns (Fig. 2) into account, the normal to the grain surface in Fig. 1 was derived to be [110] CoGa, as also schematically shown in Figs. 2(c) and 2(d). Furthermore, the diffraction patterns were analyzed in detail. For example, for each of the two SAED patterns of Fig. 2, Table II shows the number of the original negative, the experimental sample tilt angles (*x;y*), the calculated direction **B** of the electron beam and the (*hkl*) indexing of the three reflections closest to the zero spot, all for each of the two materials, CoGa and β–Ga_2O_3.

From an evaluation of these and other diffraction patterns, all taken from the sample region shown in Fig. 1, the following orientation relationship was deduced:

$$(20\bar{1})\ \beta\text{–}Ga_2O_3 \parallel (110)\ CoGa \quad ;$$
$$[010]\ \beta\text{–}Ga_2O_3 \parallel [001]\ CoGa \quad . \qquad (1)$$

Figures 2(c) and 2(d) are drawn under the assumption that Eq. (1) is exactly fulfilled. However, a close inspection of Figs. 2(a) and 2(b) (and other diffraction patterns) shows that small angular deviations (up to about 2.5°) from this orientation relationship occur. Moreover, Figs. 2(a) and 2(c) show that the (100) plane of β–Ga_2O_3 makes a small angle (about 5°) with the (100) plane of CoGa, whereas Figs. 2(b) and 2(d) reveal that the (010) plane of β–Ga_2O_3 is almost exactly parallel to the (001) plane of CoGa. We may therefore suggest that small deviations from Eq. (1) occur and that the second part of Eq. (1) is the fundamental orientation relationship:

$$(010)\ \beta\text{–}Ga_2O_3 \parallel (001)\ CoGa \quad . \qquad (2)$$

According to a LEED-study[8] on the very early oxidation state of CoGa under high vacuum conditions (100) β–Ga_2O_3 was reported to be exactly parallel to (100) CoGa (see Fig. 3 below), but in our case this is only approximately true.

The following values of the interplanar distances and lattice mismatches for the three principal space directions were calculated assuming that the orientation relationship Eq. (1) is exactly fulfilled.

Misfit in the direction [001] of CoGa [i.e., to the left in Fig. 2(d)]:

$$d(010)\ \beta\text{–}Ga_2O_3 = 0.3037\ nm$$
$$d(001)\ CoGa = 0.2878\ nm \qquad f_1 = +5.4\%$$

Misfit in the direction [110] of CoGa [i.e., downwards in Figs. 2(c) and 2(d)]:

$$d(40\bar{2})\ \beta\text{–}Ga_2O_3 = 0.2340\ nm$$
$$d(110)\ CoGa = 0.2035\ nm \qquad f_2 = +13.9\%$$

Misfit in the direction [1$\bar{1}$0] of CoGa [i.e., to the left in Fig. 2(c)]:

$$d(402)\ \beta\text{–}Ga_2O_3 = 0.1834\ nm$$
$$d(1\bar{1}0)\ CoGa = 0.2035\ nm \qquad f_3 = -10.4\%$$

The smallest of the three values f_1, f_2, and f_3 corresponds to Eq. (2), which confirms that this relation is the fundamental one. It appears that the lattice misfit along the CoGa/β–Ga_2O_3 interface is not very small, if Eq. (1) is strongly obeyed. However, our investigations pointed to

the possible presence of two deviations from Eq. (1), both of which may contribute to a reduction of the overall misfit. (i) Twins are present in the oxide, the nature of which was not investigated in detail. In fact, the different brightness of the β–Ga_2O_3 grains in Figs. 1(a) and 1(b) (dark or bright) most probably goes back to this twinning. (ii) There are the already mentioned small angular deviations from Eq. (1), e.g., small azimuthal rotations of the β–Ga_2O_3 lattice around the [010] β–Ga_2O_3 ∥ [001] CoGa axis. The orientation relationship reported in Ref. 8 is such an orientation. As an example of the orientations resulting from small rotations, Fig. 3 shows a schematic diagram of the situation described in Ref. 8, i.e., when (100) CoGa ∥ (100) β–Ga_2O_3. The (100) surface of a CoGa grain is drawn horizontally. The β–Ga_2O_3 lattice has been arranged in such a way that the (100) plane of β–Ga_2O_3 is exactly parallel to the CoGa (100) grain surface.[8] The "viewing direction" (perpendicular to the plane of the paper) is [010] β–Ga_2O_3 ∥ [001] CoGa, so Eq. (2) is obeyed. The orientation drawn in Fig. 3 deviates from Eq. (1) by about only 5°. A detailed consideration shows that the situation of Fig. 3 results in small misfit values. In summary, small deviations from the three-dimensional orientation relationship Eq. (1) may occur in the form of twins or small angular rotations.

As a result of these investigations, the following should be pointed out. If small rotations and the presence of twins are neglected, the three-dimensional crystallographic orientation of the β–Ga_2O_3 scale with respect to

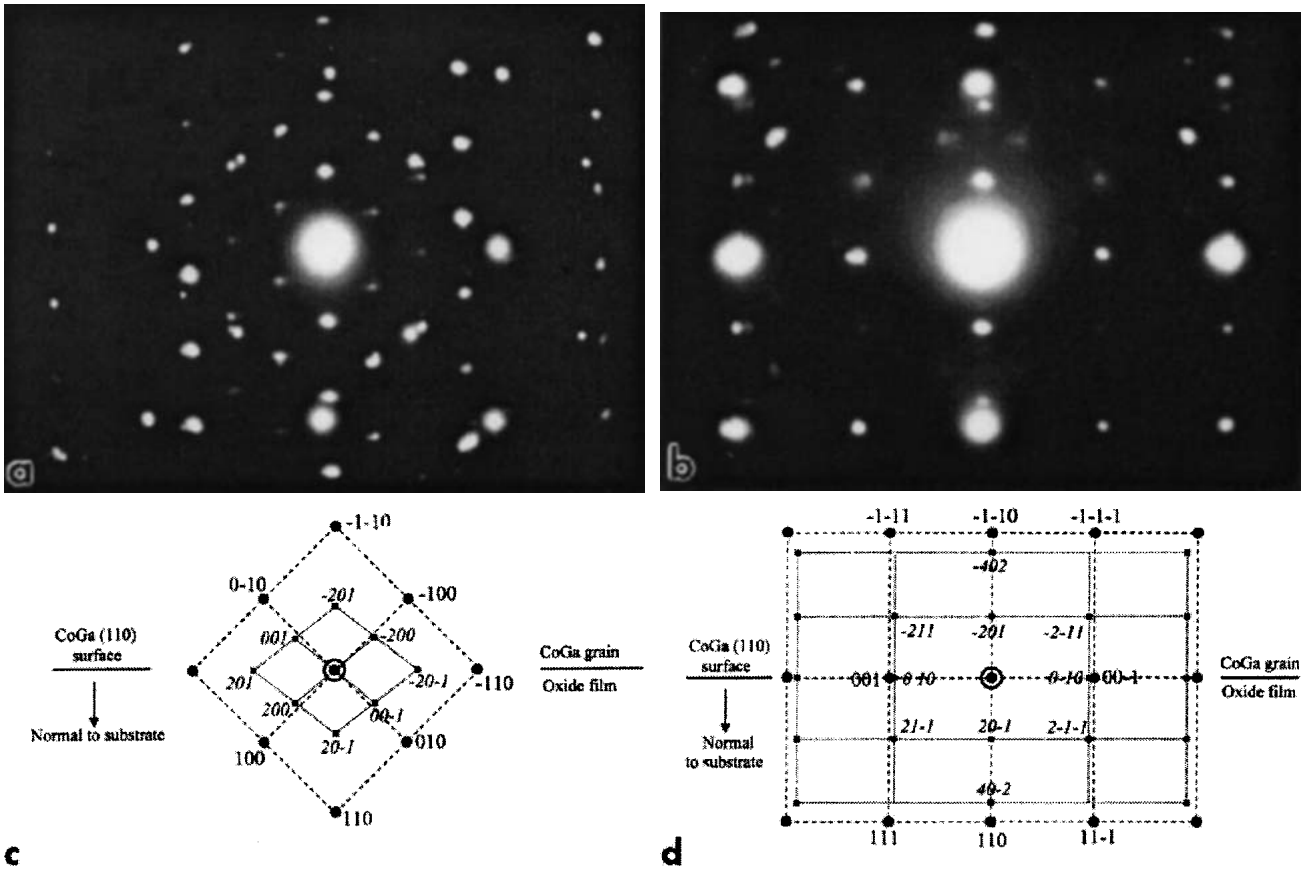

FIG. 2. (a,b) Two selected-area diffraction patterns taken at different sample tilt angles from the sample region visualized in Fig. 1. (c,d) Corresponding schematic drawings showing the calculated indexing and the assignment of the spots to the CoGa (●) and the β–Ga_2O_3 phase (■), respectively. The *hkl* indices for CoGa are given in roman letters, for β–Ga_2O_3 in italic letters. The beam direction in (a) and (c) is [00$\bar{1}$] CoGa ∥ [0$\bar{1}$0] β–Ga_2O_3, (b) and (d) it is [1$\bar{1}$0] CoGa ∥ [102] β–Ga_2O_3. Note that there is an angle of 90° between the beam directions of (a) and (b). For other details, see Table II.

TABLE II. Parameters of the SAED patterns shown in Fig. 2.

Figure no.	Negative no.	(*x*;*y*)	**B** (CoGa)	**B** (β–Ga_2O_3)	Closest spots (CoGa)	Closest spots (β–Ga_2O_3)
Fig. 2(a)	×304	(–45°; +12°)	[001]	[010]	010, 110, 100	200, 001, 20$\bar{1}$
Fig. 2(b)	×302	(+45°; +12°)	[1$\bar{1}$0]	[102]	001, 110, 111	010, 20$\bar{1}$, 21$\bar{1}$

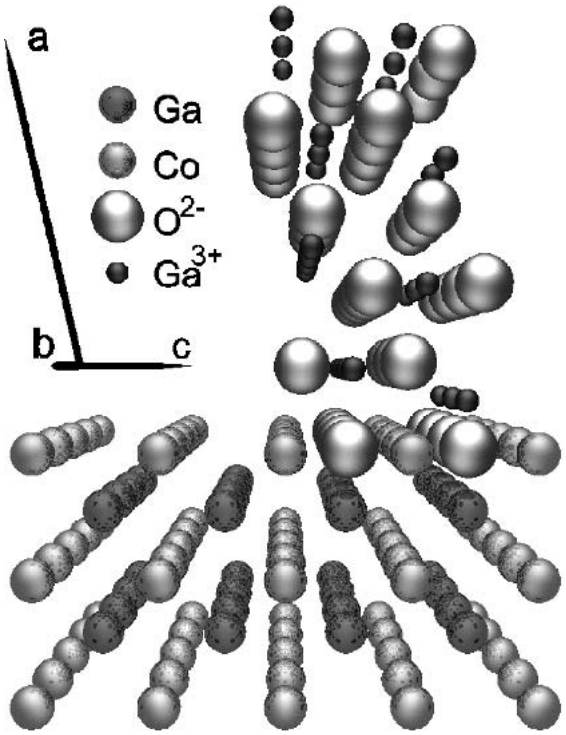

FIG. 3. Schematic drawing showing the arrangement of the atoms near a (100) CoGa/(100) β–Ga_2O_3 interface constructed in accordance with Eq. (2). The crystallographic axes of β–Ga_2O_3 (top) are shown in the upper left.

the CoGa lattice is given by Eq. (1) for all CoGa grains of the sample. This makes it most probable that a topotaxial reaction mechanism occurs. The crystallographic indexing (*hkl*) of the metal/oxide interface is, of course, different from grain to grain; i.e., the indexing of the top and bottom plane of the β–Ga_2O_3 scale depends on the indexing of the underlying CoGa surface plane. With respect to the scale growth rate, it is worthwhile to point out that the direction into which the gallium ions have to diffuse (through the growing oxide scale) is roughly perpendicular to the CoGa grain surface and that the corresponding direction in the β–Ga_2O_3 lattice of the scale varies from grain to grain. It is thus reasonable to expect corresponding variations from grain to grain in scale growth kinetics and oxide scale thickness.

2. Oxide scale thickness

TEM cross-sectional investigations allow a precise determination of the scale thickness while SAED provides information on the grain orientation. It is thus possible in principle to determine the scale growth kinetics as a function of the grain orientation by TEM and SAED. However, this requires a large number of cross sections of different regions of the same sample to be prepared, and moreover, the investigation of different samples oxidized for different times is necessary. Since this procedure is by far too elaborate, this method was applied to one only sample, in order to find out whether indeed differences in scale thickness from grain to grain occur.

Figures 4 and 5 show TEM images of the β–Ga_2O_3 scale grown on two different CoGa grains of the same sample oxidized at 800 °C for 48 h, as well as some of the SAED patterns used to determine the crystallographic indexing of the surface normal of each CoGa grain. The sample regions shown in Figs. 4 and 5 were part of the same TEM sample; the grains had a mutual separation of several hundred micrometers. Carefully studying a large section of each grain and finding sample regions where the scale had not been attacked during ion thinning confirmed that, indeed the entire scale thickness is visualized in Figs. 4 and 5. The fact that the scale surface was not affected during the ion thinning process (i.e., during TEM sample preparation) can also be deduced from the glue residues still present on the surface of the scale in both images. Whereas the scale shown in Fig. 4 has a thickness of 260 nm, the one in Fig. 5 is only 130 nm thick—a surprisingly large difference, by a factor of two, on parts of the same sample. The SAED investigation showed that the CoGa direction perpendicular to the grain surface was [$1\bar{1}0$] in Fig. 4, whereas it was [$3\bar{1}0$] in Fig. 5 (see the given SAED patterns).

Since the angle between the [$1\bar{1}0$] and [$3\bar{1}0$] directions in CoGa is only 26.6°, the above result shows that an angular difference of only 26.6° in the orientation of the CoGa surface results in a decrease of the oxidation kinetics by as large as a factor of two. Such a drastic effect can only be explained by two different crystallographic orientations of the β–Ga_2O_3 scale in Figs. 4 and 5 in accordance with the discussion in the previous paragraph. This observation was the starting point for the more detailed investigations of the growth kinetics in dependence on grain orientation presented in Sec. III.B and III.C.

3. Pore shape and size

Due to the selective oxidation of gallium from the intermetallic compound CoGa to form β–Ga_2O_3, pores are formed on the metal side of the metal/oxide interface (compare with Fig. 1). For the detailed reaction mechanism involving the formation of pores, see Ref. 2. The TEM investigations on cross-sectional samples were also used to answer the question whether such pores are already present in the early stage of the oxidizing reaction, and if so, to visualize them and to study their shapes and sizes.

As can be deduced from Figs. 4 and 5 above, these pores at the CoGa/oxide interface tend to partly adopt a crystallographic shape, whereby the pores in different CoGa grains have clearly different shapes. For example, in Fig. 4 the pore shape is rounded with a more or less

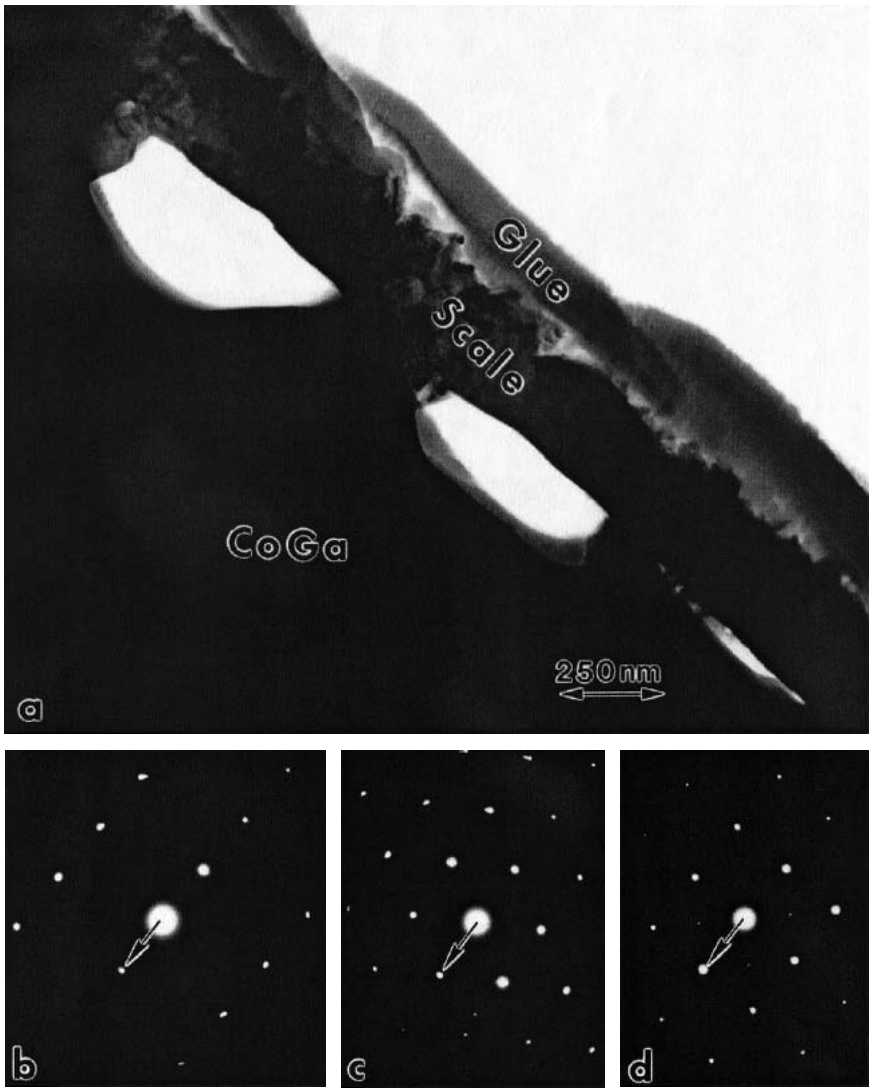

FIG. 4. (a) Cross-sectional TEM bright-field image of a scale grown on a CoGa grain having the normal to the surface along the [1$\bar{1}$0] CoGa direction, and (b–d) three corresponding SAED patterns of the CoGa grain obtained under various sample tilt angles. Tilt is around the normal to the CoGa surface plane. The beam direction is [113] in (b), [$\bar{1}$ $\bar{1}$1] in (c), and [001] in (d). In all SAED patterns, the reciprocal vector **g** = (1$\bar{1}$0) is marked by an arrow and is perpendicular to the surface plane in (a). Scale grown during 48 h at 800 °C in air. Note the pores and their shape.

flat part of the inner surface pointing to the interior of the grain, whereas in Fig. 5 the shape is roughly triangular, with an oblique corner pointing into the depth of the grain. Finally, in Fig. 1 (showing, however, a sample different from the one in Figs. 4 and 5) the pore is more lens shaped. It is reasonable to assume that the shape of the pores is determined by the orientation of the CoGa grain. Accordingly, it can be assumed that qualitative differences in the orientations of various grains can already be noticed by observation of the pore shape.

In TEM cross sections, the apparent lateral size of the pores varied rather extensively between 0.1 μm and more than 1 μm, depending on scale thickness and oxidation time (24 h or 48 h). This extensive variation at least in part might have been an effect of the cross-section preparation because the apparent pore size image depends on whether the pore had been cut centrally or rather peripherally during mechanical cutting. To avoid this problem, the pore sizes were also investigated using plan-view samples. Figure 6 shows the bright-field TEM image of a plan-view sample oxidized for 24 h at 800 °C. The dark areas are thick regions of one CoGa grain covered with the oxide scale, whereas the pores are visible as bright polygonally shaped regions. The pores are also covered by the oxide scale (compare with Fig. 1), and the latter appears to contain a high density of crystal defects. In the image shown, the lateral pore size varies between 0.2 and 2 μm, which is typical for this sample. Thus it appears that the above-described influence of the cross-section geometry on the

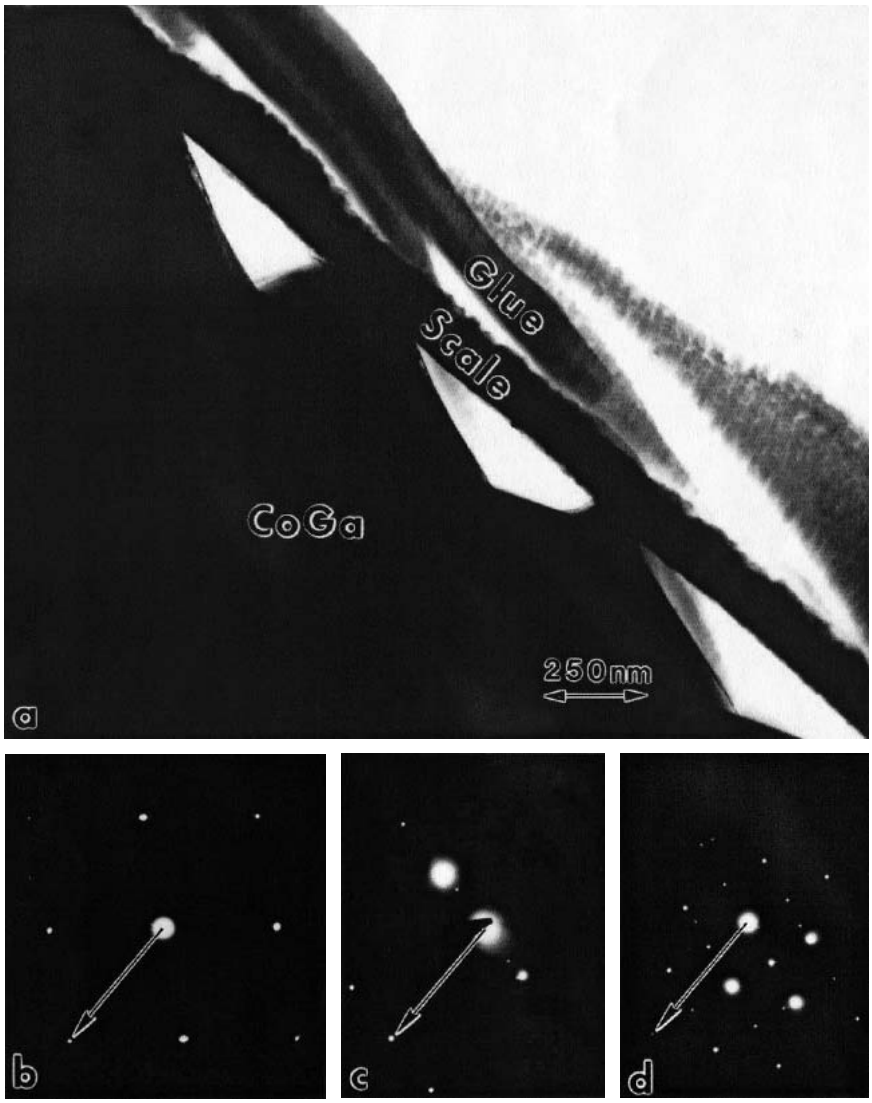

FIG. 5. (a) Cross-sectional TEM bright-field image of a scale grown on a CoGa surface having the normal to the surface along the [3$\bar{1}$0] CoGa direction, and (b–d) three corresponding SAED patterns of the CoGa grain obtained under various sample tilt angles. Tilt is around the normal to the CoGa surface plane. The beam direction is [135] in (b), [133] in (c), and [001] in (d). In all SAED patterns, the reciprocal vector $\mathbf{g} = (3\bar{1}0)$ is marked by an arrow and is perpendicular to the surface plane in (a). Scale grown during 48 h at 800 °C in air. Sample is identical to that of Fig. 4. Note the pores and their shape.

pore size determination is not important. Note also that the larger of the pores all have more or less the same shape. Again, different shapes were found on different CoGa grains (not shown).

B. Grain orientation determined by EBSD

Before an *in situ* oxidation experiment of a polycrystalline bulk CoGa-sample can be performed in an optical microscope, the crystallographic orientations of the CoGa grains to be oxidized have to be determined. For this purpose, a technique working in reflection geometry has to be used to avoid thinning of the sample. Such a method, EBSD, is available if a corresponding additional detector is present in a SEM. EBSD is capable of measuring the orientation of crystal areas relative to the laboratory coordinate system by recording the modulation of the intensity of the backscattered electrons due to diffraction at near-surface lattice planes. This intensity modulation results in patterns very similar to the Kikuchi patterns known from TEM. Figure 7 shows an example of an electron backscatter diffraction pattern obtained by SAC.

Accordingly, the same crystallographic computation methods as in TEM can be used to analyze the obtained intensity pattern and to deduce the crystallographic orientation of the crystal area investigated.[13] By analyzing several spots via a mapping function, one can cover large sample areas and obtain the different orientations of various grains in the polycrystalline sample. Such an EBSD mapping is shown in Fig. 8, where the orientations of the grains in a certain sample region, to be

oxidized subsequently in the *in situ* experiment, are determined. Two of the obtained orientations are indicated in the figure. These two orientations differ by an angle of 70.5°. Whereas the (001)CoGa plane is densely packed by either Co or Ga atoms, the (221) plane is certainly not densely packed. Thus we may expect a difference in oxidation kinetics to occur in this case.

C. Oxidation kinetics determined by *in situ* optical microscopy

Since monoclinic β–Ga_2O_3 is transparent and the refractive index is known ($n = 1.92$), the wavelengths of the colors resulting from destructive interference can be used to determine the oxide layer thickness during the oxidation process performed in the hot stage of an optical microscope:

$$\Delta x(t) = \lambda(t) \cdot \frac{2k + 1}{4n} \quad . \tag{3}$$

Here, $\Delta x(t)$ is the time-dependent scale thickness, $\lambda(t)$ the time-dependent wavelength of the color, n the refractive index, and k the order of interference, $k = 0,1,2\ldots$[14] This method was already used by Tamman;[15] however, it was performed *ex situ,* i.e., after an oxidation reaction. Our experiments were performed *in situ* at 650 °C in air, using the same sample regions for which the grain orientations had been determined by EBSD. Figure 9 shows a series of images taken during oxidation of that very area, for which the orientation determination is demonstrated in Fig. 8. The original version of Fig. 9 is in color. From video images taken at well-defined oxidation times, the colors and the corresponding wavelengths of individual grains were obtained by comparing the colors with a standard color card, and then Eq. (3) was used to derive the scale thickness.

Figure 10 shows the deduced layer thickness for the two grains visualized in Figs. 8 and 9 in a plot of the square of the thickness $[\Delta x(t)]^2$ against time t. The lines were drawn following the simple parabolic rate law

$$\Delta x(t) = \sqrt{x_0^2 + 2k_p(t - t_0)} \quad , \tag{4}$$

where k_p is the parabolic rate constant, x_0 is the thickness of the scale after an induction period of length t_0 where the oxide grows by a different rate law (nucleation, island growth, and coalescence of the islands).

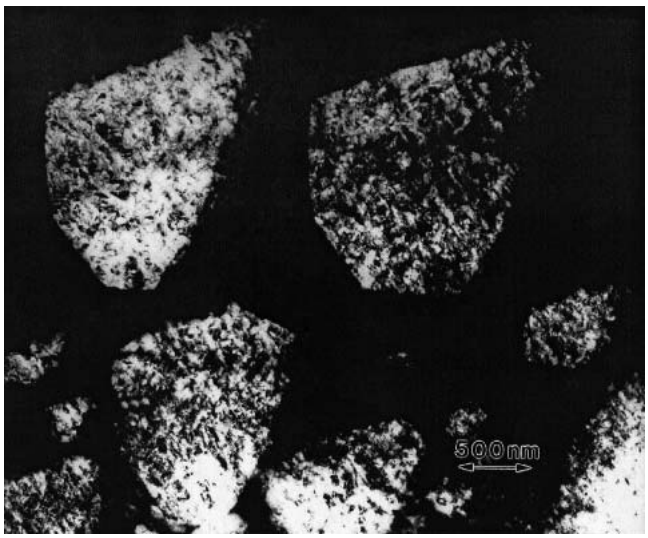

FIG. 6. Plan-view bright-field TEM image of pores in a CoGa grain covered by a β–Ga_2O_3 scale. Scale grown during 24 h at 800 °C in air. Note the different pore sizes and the most similar pore shapes.

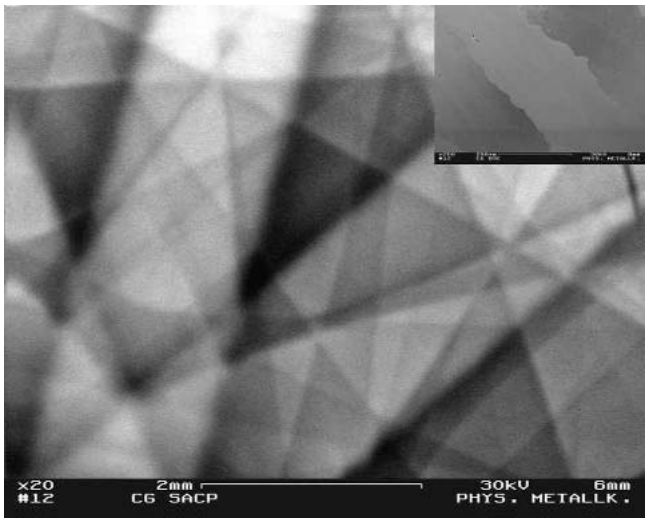

FIG. 7. EBSD intensity modulation in SEM obtained by electron backscatter diffraction from the sample area shown on top right. Note the similarity to Kikuchi patterns in TEM.

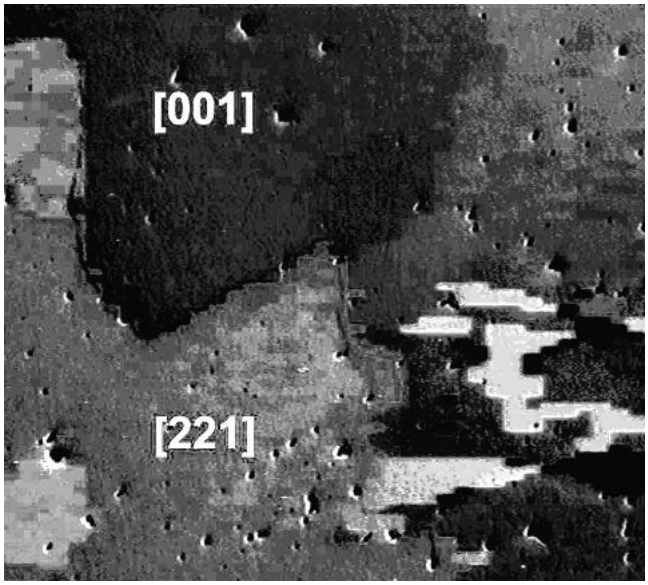

FIG. 8. EBSD map of a selected area of a CoGa sample to be oxidized. Different gray levels indicate different orientations. The [*hkl*] indices indicate the deduced normal to the sample surface. (The original image is colored. The EBSD measurements were performed by G. Frosch at Oxford Instruments, Wiesbaden, Germany.)

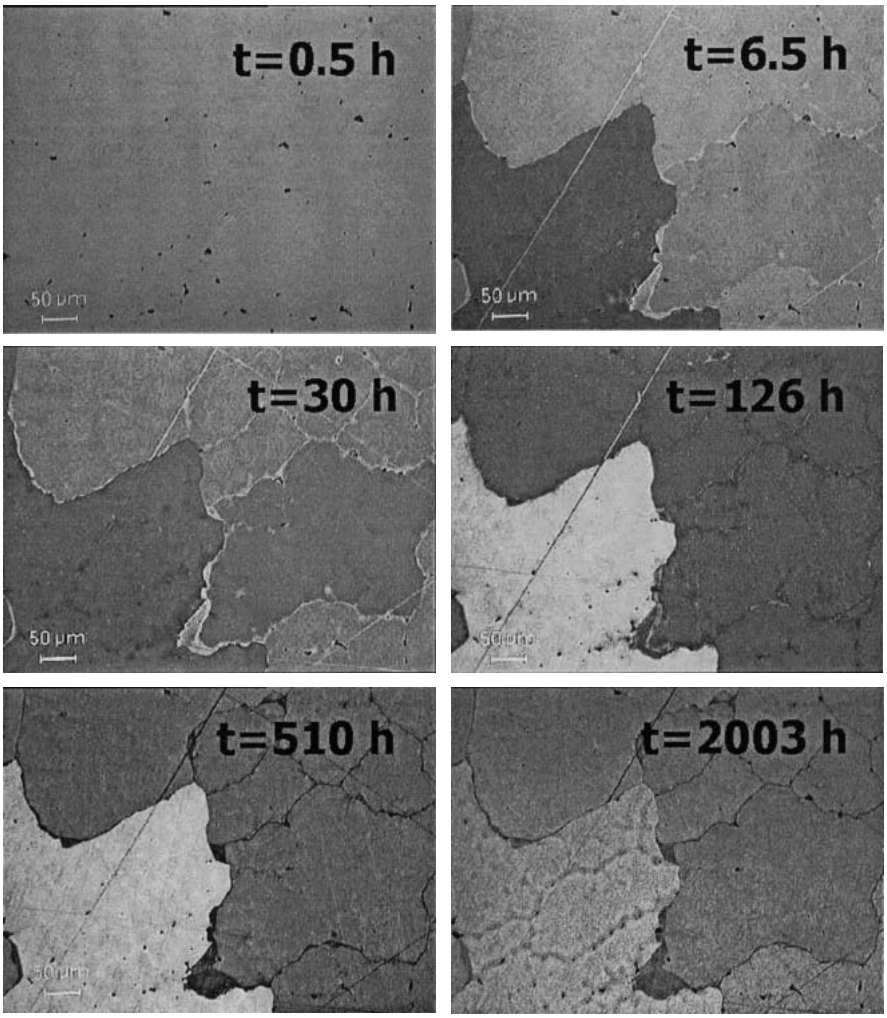

FIG. 9. Series of images taken from the CoGa area shown in Fig. 8 during *in situ* oxidation at 650 °C in air. (The original images are colored.)

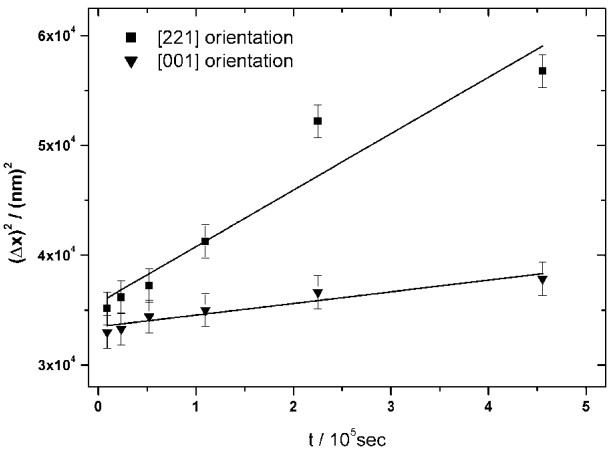

FIG. 10. Square of the scale thickness, $[\Delta x(t)]^2$, determined by *in situ* optical microscopy, in dependence on time t for the two grains shown in Figs. 8 and 9. For the lines, see the text.

From Fig. 10 it is obvious that after the induction period the β–Ga_2O_3 scale grows on both grains following a parabolic rate law, but with different parabolic rate constants for the two grains. As shown in Table III, the parabolic rate constant for the scale growth on the CoGa surface with the [221] surface normal is about five times larger than on the one with the [001] surface normal. Since the measured parabolic rate constants are smaller than the diffusion coefficients of Co or Ga in CoGa,[16] it can be concluded that the rate-determining step for scale growth is diffusion through the oxide scale and not diffusion in the intermetallic CoGa. Consequently, it can be concluded that the observed orientation effect is not due to orientation dependent mechanical damage in CoGa caused by the initial mechanical polishing. However, if

TABLE III. Parabolic rate constants of the oxidation of the intermetallic compound CoGa in dependence on the grain orientation, determined by *in situ* optical microscopy. The [*hkl*] given describe the direction of the surface normal of the grain.

Orientation	Parabolic rate constant k_P [cm^2s^{-1}]
[001]	6.3×10^{-17}
[221]	2.6×10^{-16}

the results presented in the previous section are taken into account, the drastic orientation effect can be explained by two different crystallographic orientations of the β–Ga_2O_3 scale on the two grains, leading to two different diffusion coefficients of gallium ions through the scale in the direction perpendicular to the grain surface. These results obtained *in situ* agree well with the findings obtained by TEM in Sec. III.A.2 in which scales of different thickness on differently oriented CoGa-grains were found after oxidation for a certain time. However, it was impossible to deduce the rate law for oxide scale growth from the latter findings, since no time dependence was studied. The parabolic rate law with different parabolic rate constants found in our *in situ* optical experiments confirms that after an induction period, diffusion is the rate-limiting step for scale growth. Interface control as the rate-determining step can now be ruled out, since this would result in a linear rate law.[17]

IV. CONCLUSIONS

During the high-temperature oxidation of the intermetallic compound CoGa in air, a protective oxide layer consisting of β–Ga_2O_3 is formed. Through TEM, EBSD, and *in situ* optical microscopy it was shown that during this process the crystallographic orientations play an important role. After an induction period, the growth of β–Ga_2O_3 follows a parabolic rate law with parabolic rate constants k_p depending on the crystallographic orientation of the CoGa grains. This dependence is a consequence of the anisotropy of the gallium diffusion rate through the monoclinic scale and of a topotaxial orientation relationship occurring between β–Ga_2O_3 and CoGa.

These results can be generalized, and they apply to all high-temperature oxidation processes in which oxides with anisotropic crystal structure are formed. Important examples are aluminum oxides (Al_2O_3) growing on Al-containing intermetallics, such as NiAl. As described in this paper for β–Ga_2O_3, the orientation of the anisotropic oxide scale influences the transport rate through the scale and thereby its growth rate. The orientation of the oxide is in turn controlled by the orientation of the metal grains due to topotaxial orientation relationships occurring between the metal and the oxide. Therefore the oxidation rate of the metal in effect depends on the crystallographic orientation of the surface of the metal grains.

At least two consequences of these results have to be taken into account. First, the scale thickness on a polycrystalline metal, and thus also the resistance of the metal against high-temperature oxidation, is not a uniform property but varies from grain to grain if the scale has an anisotropic crystal structure. It is thus important to study the crystal structure of the scale in detail. Second, the scale thickness on, and the oxidation resistance of a specific metal surface can be influenced at will by a specially chosen surface orientation or texture of the metal.

ACKNOWLEDGMENTS

We are grateful to G. Frosch from Oxford Instruments, Wiesbaden, Germany, for the EBSD measurements as well as O. Pompe from the Institute of Physical Metallurgy and S. Zaefferer from the Institute of Chemical Analysis, both at Darmstadt University of Technology, for the SAC measurements. We also gratefully acknowledge financial support of Deutsche Forschungsgemeinschaft (DFG MA 1090/8) for part of this work. D.H. acknowledges the support of DFG via the Coordinated Research Center SFB 418 at Martin-Luther-Universität Halle-Wittenberg, Germany.

This paper is dedicated to Professor Hermann Schmalzried on the occasion of his 70th birthday.

REFERENCES

1. U. Koops, Ph.D. Thesis, Darmstadt University of Technology, Darmstadt, Germany. (2000); http://elib.tu-darmstadt.de.
2. U. Koops and M. Martin, Solid State Ionics **971,** 136 (2000).
3. U. Koops and M. Martin, in *Mass and Charge Transport in Inorganic Materials: Fundamentals to Devices,* edited by P. Vincencini and V. Buscaglia (Techna, Faenza, 2000), pp 653–660.
4. T. Hartwig and J. Schoonman, J. Solid State Chem. **23,** 205 (1978).
5. A. Feltz and E. Gamsjäger, J. Eur. Ceram. Soc. **18,** 2217 (1998).
6. C. Wagner, Z. Phys. Chem. B **21,** 25 (1933).
7. G. Schmitz, P. Gassmann, and R. Franchy, Surf. Sci. **397,** 339 (1998).
8. M. Eumann, G. Schmitz, and R. Franchy, Appl. Phys. Lett. **72,** 3440 (1998).
9. R. Franchy, Surf. Sci. Rep. **38,** 195 (2000).
10. D.B. Williams and C.B. Carter, *Transmission Electron Microscopy* (Plenum Press, New York and London, 1996).
11. S. Geller, J. Chem. Phys. **33,** 676 (1960).
12. K. Schubert, H.L. Lukas, H-G. Meissner, and S. Bhan, Z. Metallkd. **50,** 534 (1959).
13. S. Zaeffer, J. Appl. Cryst. **33,** 10 (2000).
14. H. Kuchling, *Taschenbuch der Physik* (Fachbuchverlag Leipzig-Köln, Germany, 1995), p. 382.
15. G. Tamman, Z. Anorg. Allgemein. Chem. **111,** 78 (1920).
16. A. Bose, G. Frohberg, and H. Wever, Phys. Status Solidi **A52,** 509 (1979).
17. M. Martin, in *IUPAC Monograph: Chemistry for the 21st Century: Reactivity of Solids; Past, Present and Future,* edited by V.V. Boldyrev (Blackwell Scientific Publication, Oxford, United Kingdom, 1996), pp. 91–119.